Geophysical Prospecting

EAGE EUROPEAN ASSOCIATION OF GEOSCIENTISTS & ENGINEERS

Geophysical Prospecting, 2016, **64**, 268–286 doi: 10.1111/1365-2478.12270

Earthquake detection probability within a seismically quiet area: application to the Bruchsal geothermal field

Emmanuel Gaucher*

Karlsruhe Institute of Technology, Institute of Applied Geosciences, Division of Geothermal Research, Adenauerring 20b, D-76131, Karlsruhe, Germany

Received April 2014, revision accepted February 2015

ABSTRACT

In applications such as oil and gas production, deep geothermal energy production, underground storage, and mining, it is common practice to implement local seismic networks to monitor and to mitigate induced seismicity. For this purpose, it is crucial to determine the capability of the network to detect a seismic event of predefined magnitude in the target area. The determination of the magnitude of completeness of a network is particularly required to properly interpret seismic monitoring results. We propose a method to compute the detection probability for existing local seismic networks, which (i) strictly follows the applied detection sequence; (ii) estimates the detection capability where seismicity has not yet occurred; and (iii) delivers the results in terms of probabilities. The procedure includes a calibration of a local magnitude scale using regional earthquakes recorded by the network and located outside the monitored area. It involves pre-processing of the seismograms recorded at each station as performed during the triggering sequence, which is assumed based on amplitude thresholds. Then, the calibrated magnitude–distance–amplitude relations are extrapolated at short distances and combined to reproduce the network detection sequence. This generates a probability to detect a seismic event of a given magnitude at a specified location. This observation-based approach is an alternative to a fully theoretical detection capability modelling and includes field conditions. Seismic wave attenuation by geometrical spreading and intrinsic attenuation, site effect, and instrumental responses are partly accounted for by the calibration. We apply this procedure on the seismic network deployed in the Bruchsal geothermal field (Germany). Although the system was in good working order, no induced seismicity was identified in the area between June 2010, when monitoring started, and November 2012. The recording of distant seismicity during this time period, however, allowed the application of the proposed procedure. According to the applied network detection parameters, the results indicate that the absence of seismicity can be interpreted as a 95% probability that no seismic event with $M_L \geq 0.7$ occurred below the network at 2.4-km depth, i.e., in the geothermal reservoir.

Key words: Microseismicity, Passive seismic, Reservoir monitoring, Network design, Magnitude of completeness.

*E-mail: emmanuel.gaucher@kit.edu

INTRODUCTION

In Germany, like in many other countries, the risks associated with seismicity induced at deep geothermal fields are a serious concern, and seismic monitoring becomes a prerequisite to developing such systems. This is mainly inherited from the experience of the Basel deep heat mining project (Switzerland), which induced a $M_L = 3.4$ earthquake during water stimulation in 2006 (Deichmann and Giardini 2009) and the largely felt Landau (Germany) earthquake of $M_L = 2.7$ induced in 2009 during production from the deep geothermal reservoir (Bönnemann *et al.* 2010). Although these cases are few with regard to all operational geothermal fields in Germany, a precautionary principle is applied until the relation between the induced seismicity and the geological and operational contexts is better understood. Hence, a permanent seismic network was implemented over the Bruchsal (Germany) deep geothermal field and became operational in June 2010. This network should be able to record the seismicity induced locally by the geothermal operations, in particular by the production of the geothermal water or its reinjection, which respectively take place at depths of 2.5 km and 2 km.

Man-related operations such as mining, underground storage of fluids, enhanced oil and gas recovery, and hydraulic fracturing also require seismic monitoring to mitigate the risk associated to induced seismicity (e.g., Trifu and Fehler 1998). Therefore, the characterization of the seismic source is of main interest, and it becomes necessary to evaluate the capability of the network to detect and to locate earthquakes. The seismic network capability is defined as the minimum magnitude above which the network can detect (and locate) all earthquakes at a given area for a given period of time. It is comparable to the so-called magnitude of completeness M_C of a seismic catalogue, as long as M_C is considered space and time dependent. The knowledge of M_C exceeds the sole probabilistic (induced) seismic hazard assessment; any study based on analyses of space and time distribution of seismicity needs it as well. The characterization of the detection capability prevents from introducing bias in the data processing and interpretation, which are both related to the applied detection procedure and to the network design. In the following, we indistinctly use the terms "detection capability" and "M_C"; when the detection capability is defined in a probabilistic way, we talk about "detection probability."

Theoretical approaches and observation-based approaches can be used to estimate the detection capability of seismic networks. Freudenreich *et al.* (2012) describe a theoretical method to design a network for local monitoring purposes. The procedure couples earthquake moment magnitude with the expected ground velocities recorded at several geophones. The latter defines the background noise level at the stations and is directly connected to the detection criterion. Combining studies of Aki and Richards (1980, Chapter 4), Boatwright (1980), and Beresnev and Atkinson (1997), the authors describe the far-field body wave displacement as a function of the seismic moment (or moment magnitude) and the source time function. With this methodology, body-wave travel time, geometrical and intrinsic attenuation, density and velocity of the medium, source corner frequency, and radiation pattern must be either computed or assumed. Several of these parameters are difficult to know *a priori*, particularly the intrinsic attenuation and the seismic source time function. The effects related to the local instrumental response, such as ground coupling, sensor real sensitivity, and background noise levels are also assumed. All these sources of imprecision or inaccuracies should nevertheless be considered to provide *a posteriori* uncertainties of the modelled detection capability. Del Pezzo *et al.* (2013) applied a similar approach to estimate the magnitude detection threshold of the seismic network deployed in the Campi Flegrei area. The characterization of the background noise recorded at each station allowed them to better constrain the detection capability in the real monitoring conditions. Alternative methodologies to estimate M_C based on earthquake catalogues exist, which prevent from making several of the above assumptions and minimize some of the uncertainties existing in the theoretical approaches. However, by definition, they are only applicable to existing networks. Many of these approaches have been developed for nuclear test-ban treaty verification (e.g., Bungum and Husebye 1974; Ringdal and Kværna 1989; Sereno and Bratt 1989; Kværna *et al.* 2002). In such cases, the detection capability is typically estimated for zones located at 200 km–300 km from the seismic network, and the corresponding methodologies are therefore not so relevant for local studies. For more general applications, other techniques have been proposed to determine M_C (e.g., Gomberg 1991; von Seggern 2004; Schorlemmer and Woessner 2008; Mignan *et al.* 2011; and references therein). In the aforementioned literature, large catalogues of earthquakes exist, and in most of them, earthquakes occurred in the zone where M_C is estimated. However, in seismically quiet areas, observed catalogues of seismicity are unavailable, which prevents from applying any of the previous approach. This is the case for the Bruchsal geothermal field, which motivated the development of an alternative technique. As a matter of fact, after more than two years of monitoring (Jun. 2010–Nov. 2012), all seismic events detected by the local network

are located further than 20 km from the closest station and not in the geothermal reservoir. Yet, the absence of seismicity below the network cannot be attributed to data acquisition problems, with all seismic stations being in good working order during this period. Only little geothermal production or circulation was carried out over the monitoring period and might play a role. However, this result shall be interpreted in the light of the detection capability of the network. In the context of no detected seismicity, the determination of M_C as a function of the applied detection procedure is of primary interest. The determination of M_C associated to the location capability of the network would constitute a further step, which is not considered in this paper.

The proposed methodology can be classified in the family of the indirect estimation methods (Ringdal 1975) and was inspired by the work of Ringdal and Kværna (1989, 1992). It uses a reference catalogue of earthquakes, which are located outside the zone covered by the seismic network, to calibrate the local magnitudes as a function of the distance to each station and of the corresponding amplitudes on the seismograms. These relations are extrapolated to short distances, where no seismicity was recorded, and are combined to account for the network detection sequence. Despite its underlying assumptions, such a procedure is fully consistent with the detection processing flow and allows estimating the network detection probability before local seismicity occurs.

In the following, we first describe the characteristics of the Bruchsal seismic network and the applied detection procedure to better understand the pre-processing of the data. Then, we present the reference catalogue from which the local magnitude and the hypocentre of the earthquakes are taken. This will be used to calibrate the observed magnitude–distance–amplitude relation. Finally, we estimate the detection probability of the Bruchsal network, describe the results, and discuss the limitations and advantages of the methodology.

SEISMIC MONITORING OF BRUCHSAL

Bruchsal geothermal field

The Bruchsal geothermal field is located in Baden-Württemberg (Germany), in the Upper Rhine Graben, where a high-temperature gradient of about 50°C/km is observed (Figure 1). The hydrothermal pilot project was started in the mid-1980s and uses a well doublet. Today, a Kalina cycle power plant delivers 550 kW into the electrical network. The doublet injection and production wells are separated by approximately 1.5 km, and reach depths of approximately 2 km and 2.5 km, respectively (Herzberger *et al.* 2010). Water is produced from the Buntsandstein, Rotliegend, and Zechstein sedimentary units overlaying the crystalline basement, at a flow rate of approximately 25 L/s and at temperature of 120°C. As a result of the tectonical deformations that took place in this part of the Rhine Graben, the structure of the Bruchsal reservoir is relatively complex. It may contain several compartments corresponding to lifted-blocks separated by faults (Herzberger *et al.* 2010; Meixner 2010).

The seismic network, which has been running since June 2010, covers a surface of approximately 2.5-km radius around the middle of the well doublet. Hence, the zone located below the network contains the injection and the production wells, and corresponds to the volume within which induced seismicity would most likely initiate (Figure 1). It is composed of four stations. Each station contains three orthogonally mounted 4.5-Hz geophones installed at 100-m depth in a dedicated well. The sensor units are coupled to the formation first with sand and then with a cement cap. Distances between stations in this network range between 2 km and 4 km, and the distance between one station and one of the wellheads ranges between 900 m and 3 km. The analogue signal is digitized at 100 Hz at the surface, recorded in continuous mode, and stored in 5-min-duration files.

Network detection procedure

Once the seismic network was operating, we characterized the seismic background noise at each station in amplitude and frequency to set up the detection processing flow. Figure 2 shows a flowchart of the detection procedure, which is also applied to compute the network detection capability. Two branches are used in parallel to detect seismic event candidates within the database. First, the raw seismic traces are filtered between 4.5 Hz and 25 Hz by using a third-order band-pass Butterworth filter. This "low-frequency" branch was tuned using the closest regional earthquakes recorded by the network. In parallel, a third-order high-pass Butterworth filter above 25 Hz is applied to cover the remaining frequency range contained in the raw data. This "high-frequency" branch is expected to be more sensitive to local high-frequency radiating seismic events possibly induced in the reservoir. Here, low frequency and high frequency should be understood only as relative to the frequency content available in the seismic records (i.e., 4.5 Hz–50 Hz for a sampling rate of 100 Hz). In the rest of the paper, the raw seismic traces once filtered are called detection traces (see Figure 2).

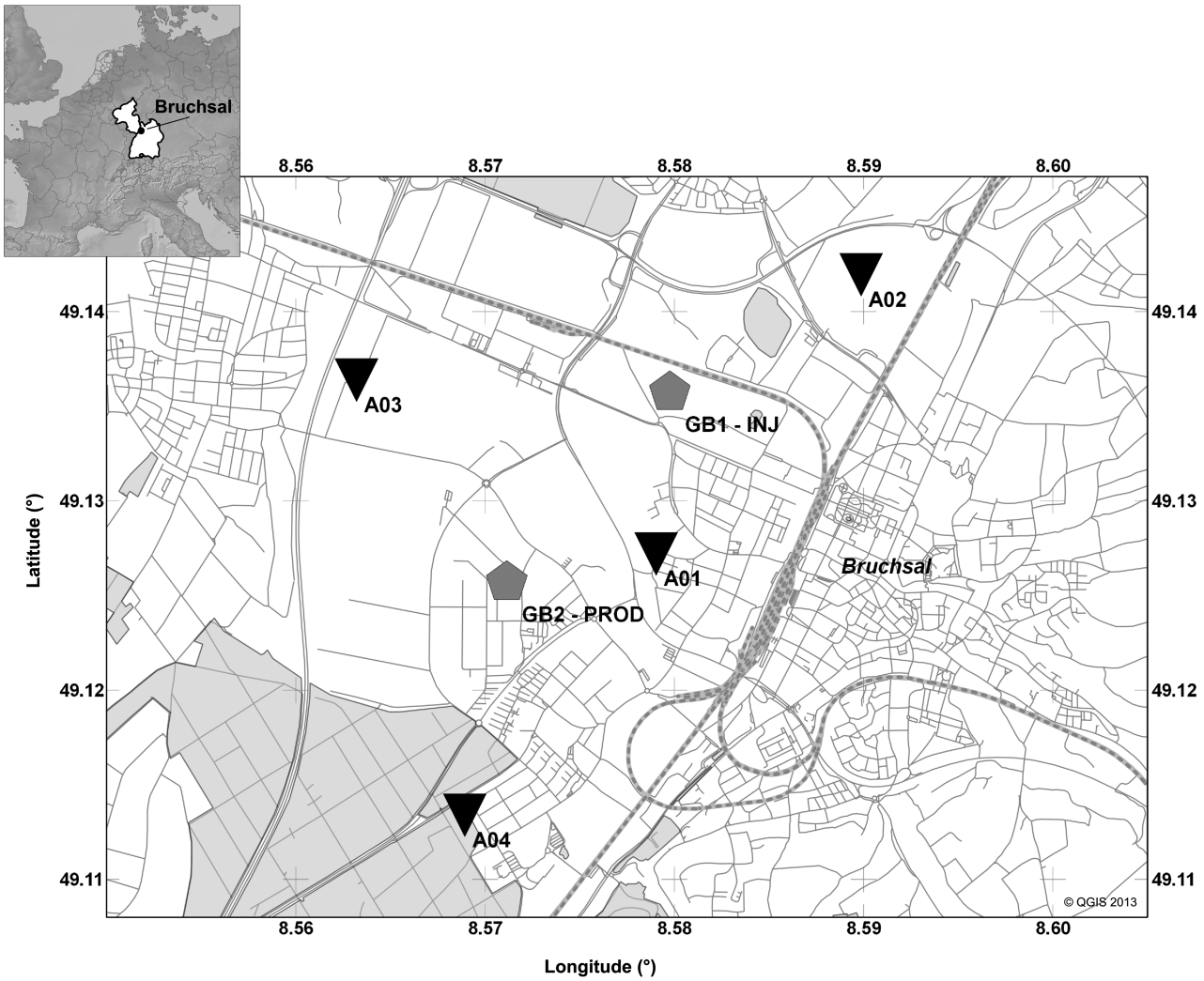

Figure 1 Map of the location of the injection and the production wells of the Bruchsal geothermal doublet (GB1 and GB2 respectively) and of the location of the four seismic stations (A01, A02, A03 and A04). The smaller map (top left corner) shows the location of the Bruchsal geothermal field more specifically with respect to the Baden-Württemberg and the Rheinland-Pfalz lands of Germany.

Once the detection traces are computed, the detection procedure applies similarly to each branch. One detection trace triggers either when its short-term average (STA) over its long-term average (LTA) is greater than 1.8 (Allen 1982; Evans and Allen 1983) or when the amplitude of the envelope of its absolute value exceeds a predefined threshold over the STA window duration (see Figure 2). The STA/LTA ratio is commonly used by software to identify and pick earthquakes (e.g., Earthworm, SeisComP). For each branch, the STA window was taken equal to four times the shortest period in the filtered seismic traces (0.16 s and 0.1 s for the low-frequency and the high-frequency branches, respectively). The LTA window lasts 50 times longer than the STA window. The use of a trace amplitude threshold in parallel to the STA/LTA threshold implies that seismic noise higher than the amplitude threshold can also trigger detection on the associated trace. During such episodes, despite many possible wrong triggers, the detection capability would however remain unchanged.

Such a detection procedure is also applied to a composite detection trace created for each station. If X_i, Y_i and Z_i are the amplitudes measured by each geophone component at time i, the corresponding value in the composite trace, hereafter called 3D-trace, is defined as $\sqrt{(X_i^2 + Y_i^2 + Z_i^2)}$. The 3D trace is expected to have good signal-to-noise ratios both for the P-wave and S-wave arrivals.

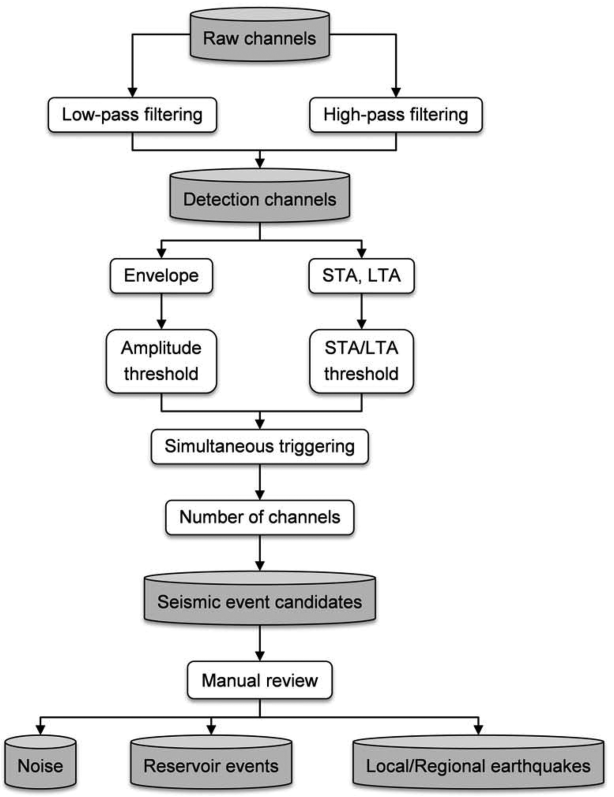

Figure 2 Schematic of the processing flow applied to the raw data to classify the records and to discriminate between noise, local or regional earthquakes, and geothermal reservoir events. This illustrates the so-called network detection.

Simultaneous triggers at several traces are required to detect a seismic event. For the Bruchsal network, ten triggers among 16 (three original traces plus the composite trace, for each station) must be activated over a time period of 2.6 s. The ten triggers correspond to a minimum of three seismic stations detecting the event on several of their traces. The 2.6-s cross-triggering window is an upper estimate of the largest time delay that can be observed between S-wave arrivals over the stations for a source located at 1.5-km depth below the network. This last step of the detection processing flow leads to earthquakes candidates, which are manually reviewed to identify possible induced events from the geothermal reservoir. As previously mentioned, at Bruchsal, no induced seismicity was identified.

For the present network, the amplitude detection threshold of each trace is determined from the associated average background noise level. First of all, the standard deviations of each detection trace are calculated for all files recorded during the first eight months of monitoring (June 2010–February 2011). Then, using standard box-plot analysis (Tukey 1977), the upper inner fence value of the standard deviations is computed and taken as the detection threshold of the associated trace. Such a detection criterion means that earthquakes are considered isolated cases (corresponding to outlying values of standard deviations) within the whole database of continuous records. Because the background noise characteristics did not vary much after February 2011, the calculated thresholds were kept constant for each trace and applied over the whole monitoring period of interest, from June 2010 to November 2012. In Table 1 (column 3), the amplitude thresholds applied to the composite 3D-trace after 4.5 Hz–25 Hz band-pass filtering are given, for each station. The variation of this threshold over the stations reflects the differences in noise level. Hence, a factor of approximately five can be observed between the noise level of station A03, which is located near a motorway, and that of station A04.

Obviously, the amplitude thresholds for triggering at each trace could be set in a different way than what is described in the previous paragraph, but whatever the method used, the network detection capability will eventually depend on those values.

DATA PREPROCESSING

In the proposed approach, the calculation of the network detection probability requires four steps that are described in detail in the following sections. First, a catalogue of the local and regional seismicity determined by an independent network must be available. This catalogue is considered a reference for the determination of the magnitude values and the earthquake locations. Second, the amplitudes corresponding to earthquakes identified in the catalogue and recorded by the network are measured on the detection traces of each station. Third, a relation between the earthquake local magnitude from the reference catalogue, the associated amplitude, and the hypocentral distance is calibrated for each station. These three steps constitute the data pre-processing phase, which is site-specific and described in the following sub-sections. Finally, from the calibrated relations, the network detection process can be converted into a probability to detect a given earthquake magnitude anywhere in the subsurface; this will be presented in the succeeding section.

The Bruchsal reference catalogue

The catalogue of the local and regional earthquakes, which occurred since the Bruchsal seismic network operates, is a

Table 1 Values of the c_S constant of equation (3) for each station. The best solution for each minimization criterion is provided with its 95% confidence interval and its regression coefficient R. The standard deviation of the magnitude residuals for the random least absolute criterion σ_S is also given in the last column. The second column shows the number of amplitude measurements used N_{obs}, and the third column gives the fixed amplitude threshold value (in μm/s) applied during the detection procedure to the composite 3D trace after 4.5 Hz–25 Hz band-pass filtering.

			Weighted least-square			Random least-square			Random least-absolute			
Station	N_{obs}	Threshold	c_S	±95%	R	c_S	±95%	R	c_S	±95%	R	σ_S
A01	252	2.70	5.312	0.031	0.69	5.311	0.055	0.73	5.330	0.038	0.75	0.319
A02	248	1.38	5.191	0.033	0.71	5.196	0.038	0.79	5.216	0.037	0.79	0.291
A03	252	5.58	5.348	0.032	0.62	5.261	0.057	0.56	5.287	0.010	0.99	0.379
A04	252	1.08	5.476	0.033	0.72	5.494	0.037	0.80	5.501	0.033	0.81	0.274

key element of the analysis. It will be used to associate the amplitude measured on this network with local magnitudes and hypocentres of the corresponding earthquakes. Hence, a Bruchsal reference catalogue (BRC) is established from the compilation of the catalogues provided by the Rheinland-Pfalz seismological centre (LGB-RLP 2013), the German seismological central observatory (SZGRF-BGR 2013), and the European–Mediterranean Seismological Centre (EMSC 2013). In each catalogue, we selected the seismicity from June 1, 2010 to November 30, 2012. All earthquakes located between 47°N – 51°N and 6°W – 11°W were kept. This corresponds to an area of approximately 450×400 km^2 centred on Bruchsal.

Similar earthquakes may be listed in two or all three original catalogues used to compile the BRC. In such situations, to prevent from repeating the same event in the BRC, the following rules were applied. The LGB-RLP catalogue was given priority over the other two. As a matter of fact, the Rheinland-Pfalz seismological centre reports, in particular, on any seismicity occurring at the Landau and the Insheim geothermal fields located only ~30 km west from Bruchsal. The SZGRF-BGR catalogue, which gathers the information provided by all German seismological centres and, more specifically, the Baden-Württemberg (Bruchsal's state) seismological centre, was given secondary priority. Finally, earthquakes listed in at least two original catalogues but with local magnitude differences larger than 0.1 were not included in the BRC. Thereby, we considered that, beyond this magnitude discrepancy, the characteristics of one earthquake, as listed in the original catalogues, are too different to be reliable for our analysis. Figure 3 shows a map of all earthquakes listed in the resulting BRC.

The BRC contains 1522 earthquakes with $-1.5 \leq M_L \leq 4.4$ and Euclidian hypocentral distances ranging from 21 and ~300 km (Figure 4). Hence, no earthquake in the vicinity of Bruchsal is listed in the BRC. Such an observation is consistent with the fact that no seismicity was recorded below the Bruchsal seismic network.

All records of the Bruchsal seismic network corresponding to the BRC earthquakes were manually checked. Following the automatic detection procedure applied on the continuous records, about 3% of the BRC earthquakes were automatically detected (green circles in Figure 4). All automatically detected earthquakes were identified by the low-frequency processing branch, whereas less than 30% of them were also seen by the high-frequency processing branch. Others were not automatically detected but could be identified, *a posteriori*, by looking at the corresponding seismogram (orange circles). The procedure missed these events either because the filtering of the raw seismic traces was not adapted to the furthest events or because the signal was not strong enough to trigger the required number of traces. Finally, the remaining earthquakes of the BRC were not visible at all on the corresponding seismograms recorded by the network (red circles). As expected, the detected events belong to the upper part of the plot, whereas the missed ones belong to the bottom part, and the visible but not detected events are in-between. The lower limit of the distribution of the detected (and visible) events follows, at first order, a linear relation between the local magnitude and the logarithm of the hypocentral distance, as would apply in a homogeneous propagation medium without signal intrinsic attenuation.

Such magnitude–distance plots are used by Schorlemmer and Woessner (2008) to estimate the detection probability of the Southern California Seismic Network. For each station of the network, the ratio between the detected and undetected earthquakes for predefined cells in the magnitude–distance plane will define the probability for a single station to detect. This observation-based approach cannot be applied at Bruchsal because: (i) it estimates the detection capability only for

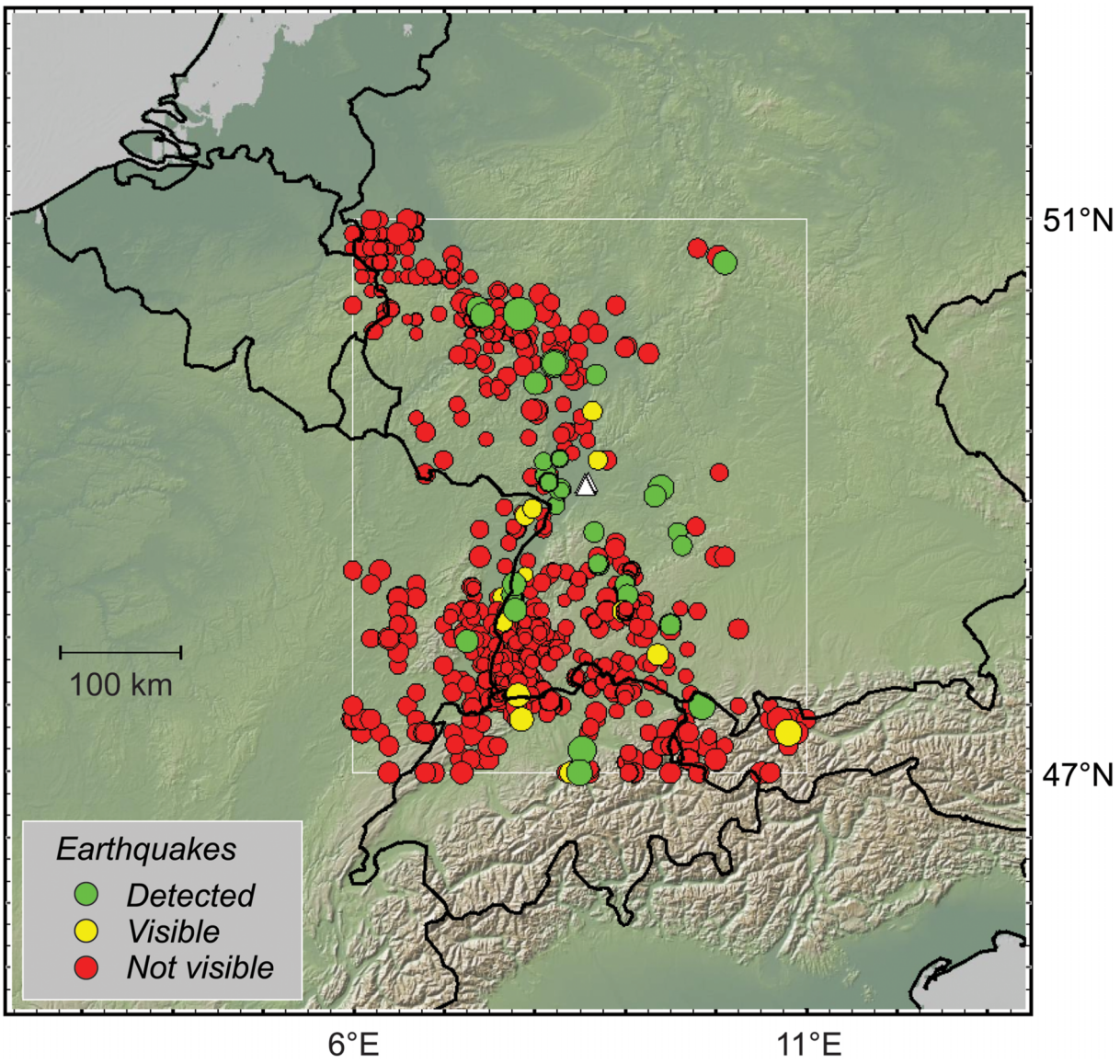

Figure 3 Epicentre map of all earthquakes of the BRC, which results from the compilation of the LGB-RLP, SZGRF-BGR, and EMSC catalogues for the 1-Jun-10 to 30-Nov-12 period and for the zone limited by the white rectangle. The green circles represent the earthquakes automatically detected by the Bruchsal network (white triangles), the orange circles represent those that were not detected but are visible on the corresponding seismogram, and the red circles represent the earthquakes not visible on the seismogram. The circle size is proportional to the earthquake magnitude.

distances corresponding to observed seismicity, and (ii) the detection procedure only considers the presence or absence of stations in the network. On the contrary, we need to find a magnitude–distance relation, which could be extrapolated anywhere, particularly close to the network where no seismicity was identified, and which would depend on the triggering criterion at each trace.

Calibration of the magnitude–distance–amplitude relation

By following Stange (2006), the local magnitude measured at one station can be written

$$M_L = \log\ A_{WA} + a \times \log\ r + b \times r + c_s, \quad (1)$$

with A_{WA} being the mean Wood–Anderson amplitude of the horizontal components in mm, r the Euclidian hypocentral

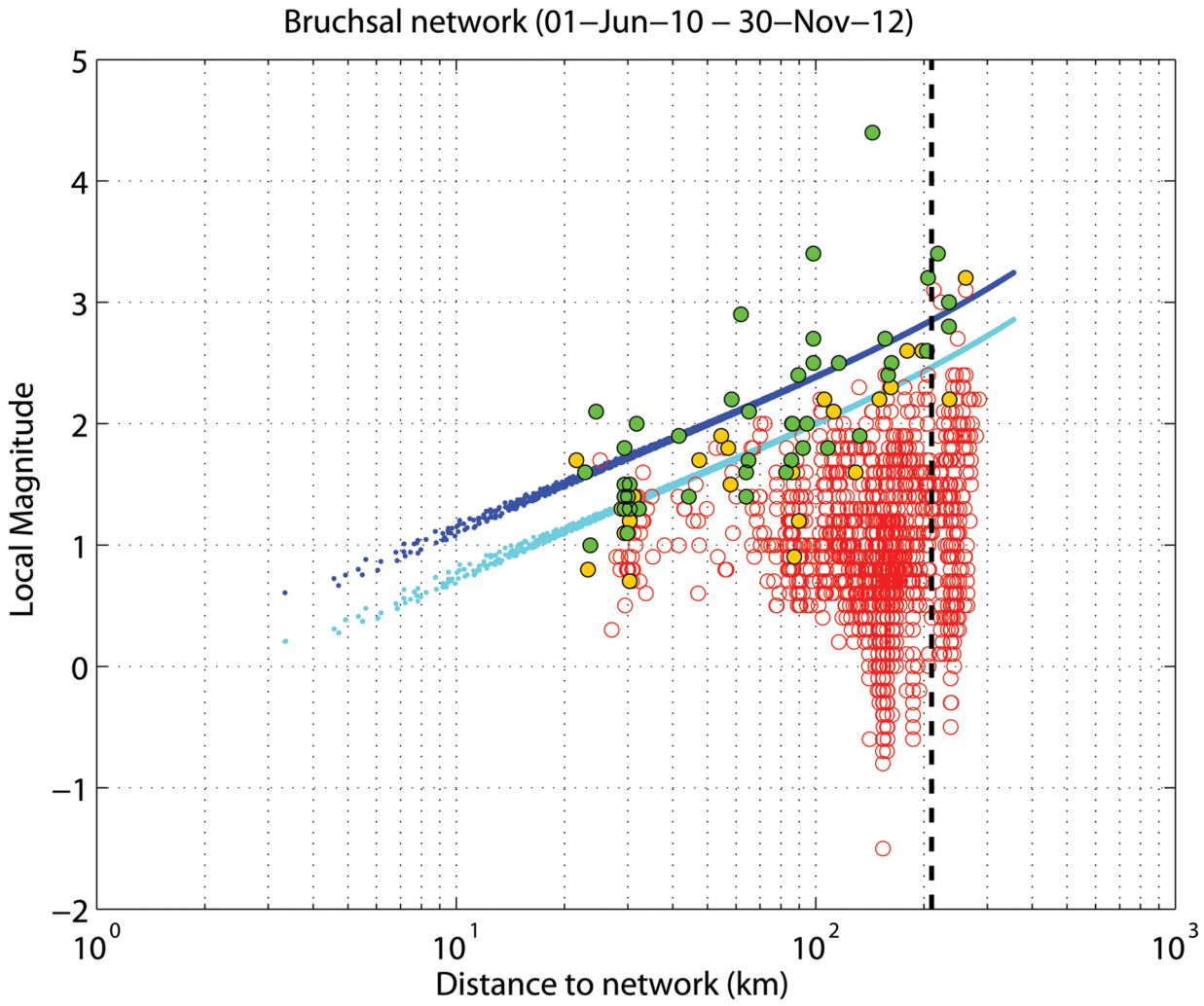

Figure 4 Magnitude–distance distribution of all earthquakes of the BRC. The green circles represent the earthquakes automatically detected by the Bruchsal network, the orange circles represent those that were not detected but are visible on the corresponding seismogram, and the red empty circles correspond to the remaining earthquakes of the BRC not visible on the corresponding seismogram. The cyan-scattered and blue-scattered points represent the detection capabilities of the network, with 50% and 95% probabilities respectively, computed as described in the section "Detection probability of the Bruchsal seismic network." The vertical black dotted line shows the distance upper limit of the calibration of the magnitude–distance–amplitude relation.

distance measured in km, and a, b and c_S constants. Since hypocentral distance is considered, we are unable to identify possible depth-specific contribution to the local magnitude. This equation is consistent with the local magnitude scale as proposed originally by Richter (1935) and new forms reviewed in Bormann (2012). The terms at the right of the log A_{WA} correspond to the so-called distance correction factor. Indeed, $a \log r$ can be associated with the geometrical spreading of the seismic waves, $b\, r$ to the wave intrinsic attenuation and the last constant to a station-dependent level. Stange (2006) calibrated equation (1) for the state of Baden-Württemberg and obtained:

$$M_L = \log A_{WA} + (1.11 \pm 0.1) \log r + (9.5 \pm 2.0) \times 10^{-4}\, r + (0.69 \pm 0.05). \quad (2)$$

Equation (2) is used by the seismological centres (LGB-RLP and SZGRF-BGR) to compute the local magnitudes—provided in the catalogues—of earthquakes located in

Rheinland-Pfalz and Baden-Württemberg (Stange 2014, pers. comm.). Consequently, it is suitable for Bruchsal. However, it cannot be applied in the present form to compute the value of M_C as a function of the detection procedure we apply on the raw data. Indeed, there is no simple relation between the Wood–Anderson amplitude and the amplitude as read on a detection trace. Yet, the latter controls the network detection. Therefore, to be consistent with the detection sequence, we modified equation (2) as follows. The Wood–Anderson amplitude was replaced by the amplitude of the detection trace (Figure 2), and the resulting equation was applied to each detection trace. A single set of equations would apply for each frequency domain ("low" and "high") of the detection traces. With this formulation, no correction of the geophone effective response, integration of the velocity measurement, and application of the original Wood–Anderson response were performed unlike what would have implied the formal application of equation (2). However, this assumes that the removal of the Wood–Anderson conversion and all other considered amplitude changes only affects the constant value of the right term of equation (2), in each frequency domain.

The calibration of equation (1) was done by fixing the amplitude-independent a and b parameters to their average values in equation (2) in order to comply with the distance correction factors calibrated by Stange (2006). Therefore, only the constant parameters c_S must be optimized. This was performed for each station independently. Hence, for Bruchsal, the local magnitude equation becomes

$$M_L = \log\ A_{DC} + 1.11 \log r + 9.5 \times 10^{-4}\, r + c_S, \qquad (3)$$

with A_{DC} being the amplitude measured on the detection trace (in m/s).

From the identified events of the BRC (green and orange circles of Figure 4), the maximum amplitudes of the detection traces were measured. This was carried out only for the Pg and the Sg seismic wave arrivals and for seismograms where no Pn phase was observable. This selection criterion was applied to obtain reliable measurements and to better suit local scale analysis. In practice, all earthquakes further than ~210 km from the network were discarded from the analysis. Hence, only 63 earthquakes remained for the analysis and all derived from the German catalogues (90% from the LGB-RLP and 10% from the SZGRF-BGR). The maximum amplitudes of the P-wave and the S-wave were measured on the traces after applying the 4.5 Hz–25 Hz band-pass filter (Figure 5). The low-frequency branch was selected because 100% of the detected events originate from it compared with 30% for the high-frequency branch and, therefore, better constrains the problem in the rest of the procedure. The background noise prior to the P-wave arrival was also measured. It was quantified by the 95% percentile of the trace amplitude computed before the P-wave maximum, over a window of S minus P time duration. Indeed, for several traces (those which did not effectively trigger), the P-wave and S-wave onsets have amplitudes close to the background noise level (e.g., all four components of station A03, see Figure 5). Therefore, the noise perturbation on the measured P-wave and S-wave amplitudes must be accounted for, and the noise level will be later used to weight the observations during calibration.

Only the S-waves were processed because they are most of the time the strongest arrivals within the seismograms recorded at Bruchsal (88% of the S-wave amplitudes were stronger than the P-wave amplitudes). Thus, S-wave onsets are better representatives of the triggering and the effective detection of a seismic event candidate at Bruchsal. S-wave amplitudes stronger than P-wave amplitudes for local seismicity may be observed in other places (e.g., Soultz-sous-Forêts geothermal field); hence, it is not unrealistic to also keep this assumption for shorter distances. Linear fitting was carried out between the magnitudes of the catalogue (left term of equation (3)) and the distance correction factor (right term of equation (3)), which can be computed from the measured amplitudes and the distances. We used three minimization criteria. First, weighted least-squares were applied. The weight was chosen proportional to the inverse of the noise level measured for each trace and was set to 0 when the amplitude-to-noise ratio was below 1. Second, instead of applying weights, the amplitudes were randomly perturbed according to a normal distribution with standard deviation equal to half the associated noise. Then, for each of the 10,000 random draws, fitting was made using either least squares minimization or least absolute minimization. Finally, the median of the 10,000 results was kept as the best solution. Table 1 shows the solutions obtained for the different fitting criteria. As observed, for the stations A01, A02 and A04, all computed c_S values stand within the 95% confidence level of each minimization criterion. Only station A03 exhibits larger discrepancies of c_S. However, when rounded to one decimal unit (0.1 point in magnitude), all methods provide the same result. Interestingly, mainly for the stations A01 and A03, the random least absolute fitting criterion improves the regression coefficients and decreases the 95% confidence levels compared with the random least squares criterion. These two stations, which are the noisiest of the network (see column 3 of Table 1), had fewer observations, as indicated by the number of used amplitudes (see column 2 of Table 1). Hence, they are

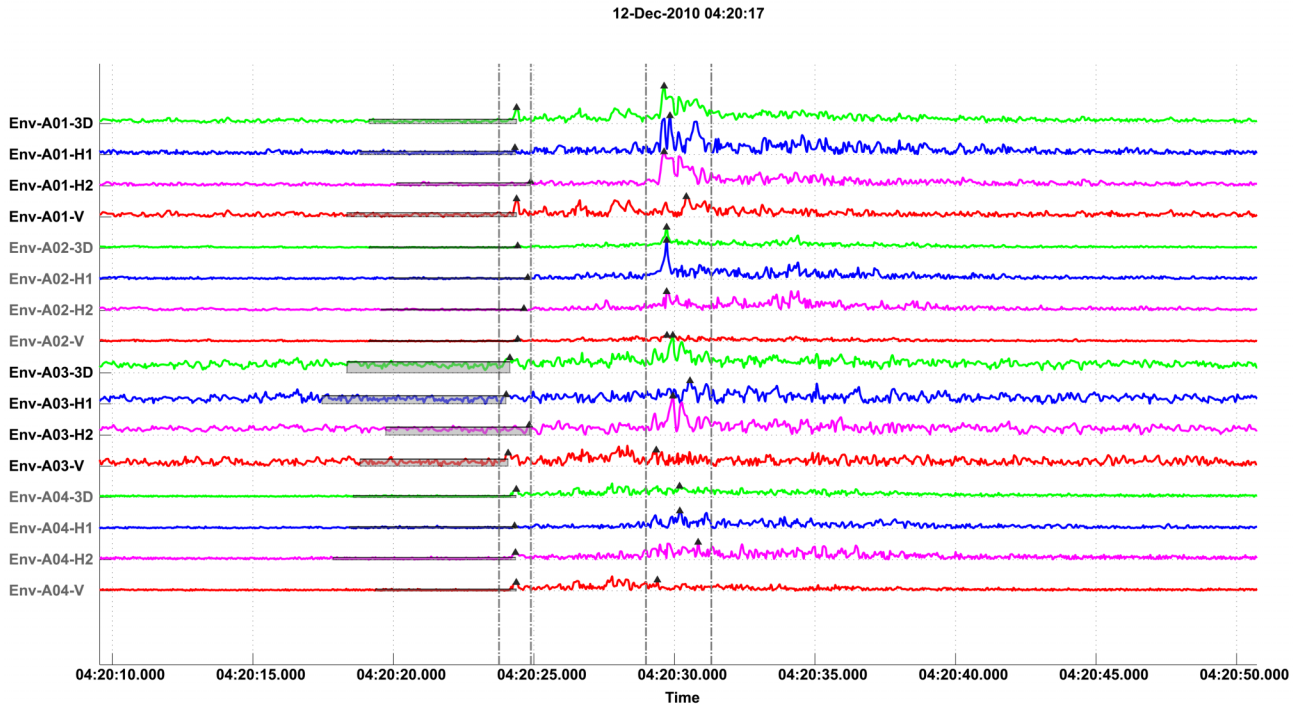

Figure 5 Example of amplitude picking of the low-frequency detection traces of Bruchsal network. For each monitoring stations (A01, A02, A03, and A04), four triggering traces are considered (see text for details). On this example, the P-wave and S-wave maximum amplitudes have been picked (black triangles) as well as the noise level before the P-wave (grey rectangle, which upper horizontal side gives the noise level). The amplitude (vertical) scale is the same for all traces.

likely to provide more outlier observations. Accordingly, we kept the values of c_S obtained by the random least absolute criterion.

Figure 6 shows the differences between the magnitudes computed using the calibrated equation (3) M_{Calc} and the BRC magnitudes M_{Obs} for each station. They follow Gaussian distributions centred on 0. The standard deviation of the residuals at each station σ_S is provided in Table 1. These values are reasonable, around 0.3, and close to the 0.2 obtained by Stange (2006). The residuals reflect the uncertainties due to the model assumptions as well as to the possible uncertainties associated to the M_L and locations listed in the BRC catalogue. It is generally accepted that uncertainties of at least ± 0.1 can apply on M_L of catalogues.

DETECTION PROBABILITY OF THE BRUCHSAL SEISMIC NETWORK

Method

The approach to determine the network detection probability is close to that proposed by Ringdal and Kværna (1989, 1992) for the continuous threshold monitoring. In this study, however, no time variation of the thresholds is considered since they have not been changed during the covered monitoring period, but such a case could be implemented by repeating the procedure each time the thresholds are updated.

In a first step, the subsurface is discretized on a regular mesh, and the distance from every node to every station is computed. Then, for every trace belonging to one station, the corresponding detection threshold is taken as the amplitude value in equation (3), and the associated threshold magnitude is calculated for each node of the mesh. Applying the calibrated equation (3) however leads to uncertainties in the magnitude determination, as shown by the residuals obtained in the previous sub-section (see Table 1 and Figure 6). Therefore, to quantify the probability to correctly estimate the magnitude of an event from equation (3), the Gaussian distribution characteristics of the residuals are used. Thus, for each detection trace, the probability that the real magnitude of an event M_{Obs} is smaller than the estimated magnitude M_{Calc} is defined by

$$P(M_{Obs} \leq M_{Calc}) = G(M_{Calc}/\sigma_S), \tag{4}$$

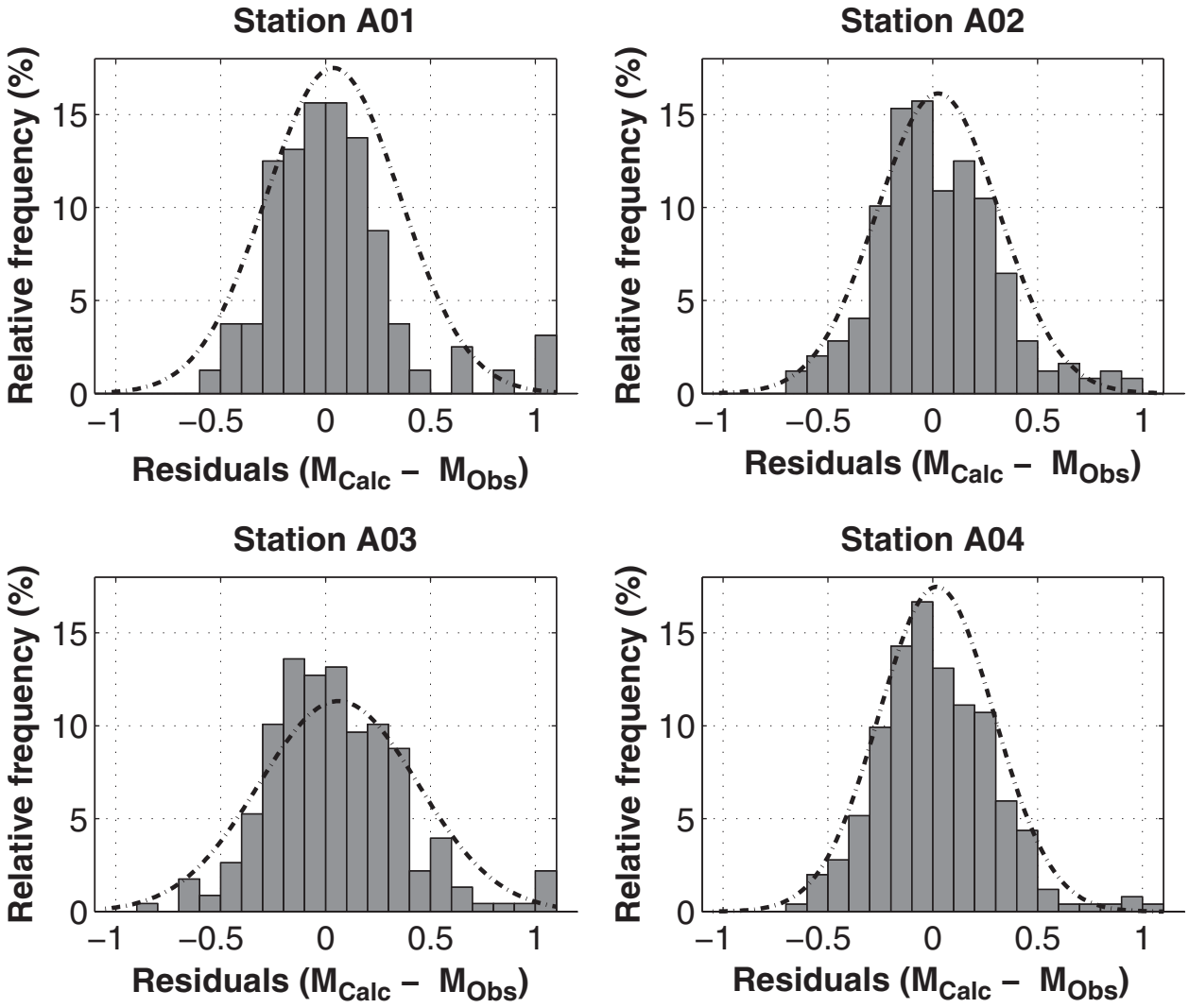

Figure 6 Histogram of the magnitude residuals at each station (grey bars), overlaid by the corresponding Gaussian distribution (black curve).

with G being the cumulative Gaussian distribution function and σ_S the standard deviation of the residuals at each station (Ringdal 1975). Equation (4) indicates that the magnitude computed from equation (3) has 50% probability to be correct. Only if σ_S would be 0 (no residuals) that the calculated magnitude would perfectly match the observed magnitude and the probability distribution in equation (4) would follow a Heaviside step function. Therefore, at each node, the probability to trigger an event as a function of its magnitude can be computed for each trace of a station. Finally, the detection capability, at each node, is the magnitude that corresponds to the highest joint probability level obtained from N_{Cha} traces supposed to simultaneously trigger. The joint probability is the product of the individual probabilities. For Bruchsal, $N_{Cha} = 10$; therefore, ten traces among 16 must simultaneously trigger to detect a seismic event candidate. This corresponds to at least three stations detecting among 4.

Because we calibrated equation (3) for each station and not for each trace, the probability distributions around the expected magnitudes are different from station to station but are similar for all traces of one station (Figure 6). This dependence means that the probability distribution associated with a given magnitude for a given trace is the same for all other traces of the station, despite corresponding to different magnitude values. It leads to higher *a posteriori* joint probabilities compared with what would be obtained from a completely

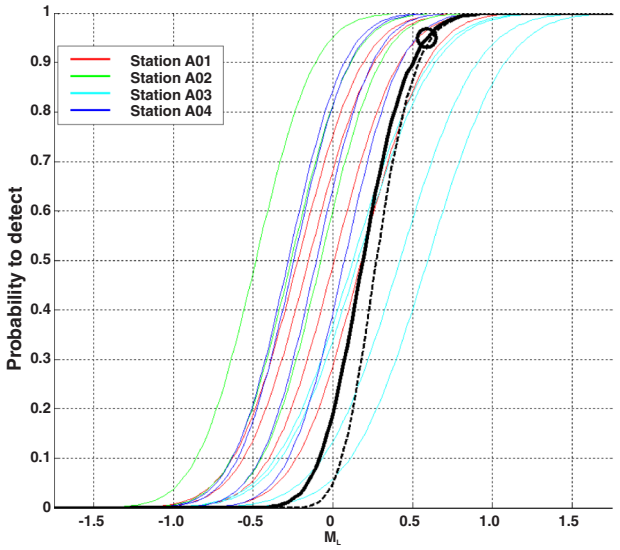

Figure 7 Probability to detect a seismic event as a function of its magnitude, for one node of the meshed target (black thick line). At this node, there is 95% probability to detect a $M_L = 0.6$ event (black circle). The probabilities corresponding to each detection trace of each station are shown (one colour per station). If the detection traces had independent probability distributions, the joint probability would be that shown by the black dashed line.

independent case. Moreover, neglecting the uncertainty in the magnitude determination (i.e., taking $\sigma_S = 0$) would lead to very optimistic detection capability scenarios.

Figure 7 highlights intermediate and final results obtained during the detection procedure, for one node of the meshed target zone. The probability to trigger for each trace is plotted as well as the joint probability obtained for the network detection (solid line) and the joint probability, which would be obtained if all traces were considered independent (dashed line).

Results

Prior to looking in details at the spatial distribution of the detection capability of the Bruchsal seismic network, its consistency with the earthquake catalogue has to be appraised. Figure 4 shows the real capabilities of the network in terms of detected, visible, and invisible earthquakes of the BRC (as discussed in section "The Bruchsal reference catalogue") overlaid by the predicted ones, with 50% and 95% probabilities (cyan and blue scattered points, respectively). Up to the calibration distance limit of ~210 km, 47% of the earthquakes listed in the BRC and plotted above the 50% probability level (cyan scattered points) have been effectively detected by the network. This percentage is equal to 88% when considering the 95% probability level (blue scattered points). In this case, only one non-detected earthquake remains above the probability curve. The validity of the corresponding $M_L = 1.7$ earthquake, located at ~25 km from the network, is however questionable. Indeed, it is not listed in the LGB-RLP catalogue but only in the SZGRF-BGR one, which is surprising according to its location and magnitude. This analysis shows that the calculated detection capability is fairly consistent with the effective results obtained on the Bruchsal network. Hence, we could also expect consistency with the results that we would obtain by applying the approach proposed by Schorlemmer and Woessner (2008), at least for distances associated to earthquakes of the catalogue.

Figure 8 shows three cross sections of the network detection capability at the scale of the Bruchsal monitoring network. A 95% detection probability level is selected. The horizontal section is taken at 2400 m to present the results obtained at the depth of the geothermal reservoir. Two vertical sections are also displayed: one along the West–East direction and one along the South–North direction. They correspond to the profiles A and B plotted on the horizontal section. As observed, close to the network and below it, the detection capability is variable. M_C strongly depends on the distance to each station as well as on the discrepancies between the trace amplitude-triggering thresholds. Hence, the iso-detection contours are neither radial nor centred on the network. The smallest detection threshold is located southwestward from A01 station, with a value of $0.55 \leq M_C \leq 0.6$, as shown on the horizontal section. Anywhere under the network footprint, which covers an area of approximately 2 km radius, there is 95% probability that an earthquake of $M_L \geq 0.7$ would be detected. Therefore, a variability of approximately 0.15 points in magnitude may be observed under the network, at 2400 m depth, depending on the event location. Obviously, variability also exists in depth as observed on the vertical sections. This emphasizes that the detection capability must be considered a location-dependent characteristic at the network scale, and M_C cannot be taken as constant below the network. Such effect decreases as the distance between the target zone and the network increases because the distance dependent term in equation (3) then dominates the others. Hence, the iso-detection contours become roughly spherical around the network. The location dependence is also highlighted in Figure 4 by the scattering of the calculated detection capabilities, particularly for distances shorter than ~20 km (cyan and blue scattered points).

The characteristics of the network detection used in the example above were applied to the Bruchsal network between

June 1, 2010 and November 30, 2012. Accordingly, the lack of detected seismicity in the vicinity of the geothermal reservoir during the monitoring period means that there is 95% probability that no earthquake with $M_L \geq 0.7$ occurred in this area.

Once the magnitude–distance–amplitude relations have been calibrated for each station, it is possible to simulate the performance of different detection scenarios. For example, the effect of losing one station during monitoring can be modelled to assess the robustness of the network design or to follow-up the variations of the effective detection capability under such circumstances. Figure 9 shows the effect of removing the central station of the network, i.e., station A01, but leaving the network detection parameters unchanged ($N_{cha} = 10$). In that case, 2400 m below the network, the detection capability gives at best $0.7 \leq M_C \leq 0.75$ and at worst $0.9 \leq M_C \leq 0.95$, with 95% probability. This means that the removal of A01 leads to increase M_C by approximately 0.15 points compared with the original network. In addition, the detection capability is no longer roughly centred on A01 but moves westward, closer to A03, which is the noisiest station, therefore the least sensitive one. Obviously, it would be possible to improve the detection capability of the network without A01, particularly by decreasing the number of required simultaneous triggers. For example, setting the simultaneous triggers to $N_{cha} = 6$ would lead to $0.35 \leq M_C \leq 0.5$ below the network. However, the detection procedure would certainly lead to many more wrong identifications of earthquakes (or false alarms), and the location capability of the network would worsen; locating with three stations is always more uncertain than locating with four stations. This example highlights that, even for one specific monitoring network, the detection procedure plays a major role in the resulting catalogue of the detected earthquakes and for the interpretation of the results in space and possibly in time. In practice, this implies a monitoring of the detection procedure itself.

Discussion

The magnitude–distance–amplitude relation plays a major role in the estimate of the network detection capability. Figure 10 (left) shows an epicentre map of all earthquakes, which were used during this processing step, as well as their hypocentral distance and azimuth to each station (right). No systematic clustering of either the distance or the azimuth between the earthquakes and the network can be observed. Hence, these characteristics of the BRC catalogue should not bias the calibration results. Additionally, due to the relatively large distance range between the network and the catalogue events, we can assume the uncertainty in the hypocentre locations to have only a minor effect on the calibration.

Equation (2), on which equation (3) is based, has been calibrated down to 10 km distances (Stange 2006) and is used to compute the local magnitude provided in the LGB-RLP and SZGRF-BGR catalogues for Rheinland-Pfalz and Baden-Württemberg earthquakes. For less than 10-km-distant earthquakes, equation (2) would still be used in these catalogues, but large magnitudes from short offset stations might be discarded (Stange 2014, pers. comm.). Hence, the M_L value used as the reference magnitude in the proposed approach remains consistent within the BRC and would still apply for distances below 20 km.

As observed in Figure 11, the BRC magnitudes larger than 3 are systematically underestimated after calibration of equation (3). This results from the minimization criterion that weights the amplitudes by the preceding noise level. Indeed, all $M_L \geq 3$ earthquakes are farther than 100 km from the network (Figure 4) and exhibit smaller signal-to-noise ratio (small radius circles). For the stations A01 and A03, it looks like the earthquakes of magnitude below 1 are systematically overestimated. Regarding the detection capability, this means keeping a conservative position. Figure 11 emphasizes also the higher noise generally observed at station A03, and to a smaller extent at station A01, compared to the other stations.

Still related to the attenuation factor, equation (3) could also be questioned. We applied the results of Stange (2006) and only seek to calibrate the regional constant and the station-dependent site effect (the c_S constant). This could have been done for each detection trace of each station in order to better represent the single trace coupling and the instrumental response differences. However, due to the low number of input data, this option was rejected. In addition, we could argue that the intrinsic attenuation parameter of equation (3), the b constant in equation (1), may still account for the Bruchsal site effects and may depend on the frequency range of the analysed data. This is relevant since the detection traces are low-frequency or high-frequency filtered traces and have, overall, relatively narrow frequency bands. Moreover, the a constant in the geometrical spreading factor may not be very adequate and could be fixed to the usually accepted value of 1 for short distances. Considering these possible variations of the a, b, and c_S constants, a couple of new calibrations were carried out and consisted in finding the best values for b and c_S keeping $a = 1.11$ or taking $a = 1$. The b constant was first optimized using all station observables because this constant is not station dependent. Then, the c_S constant was

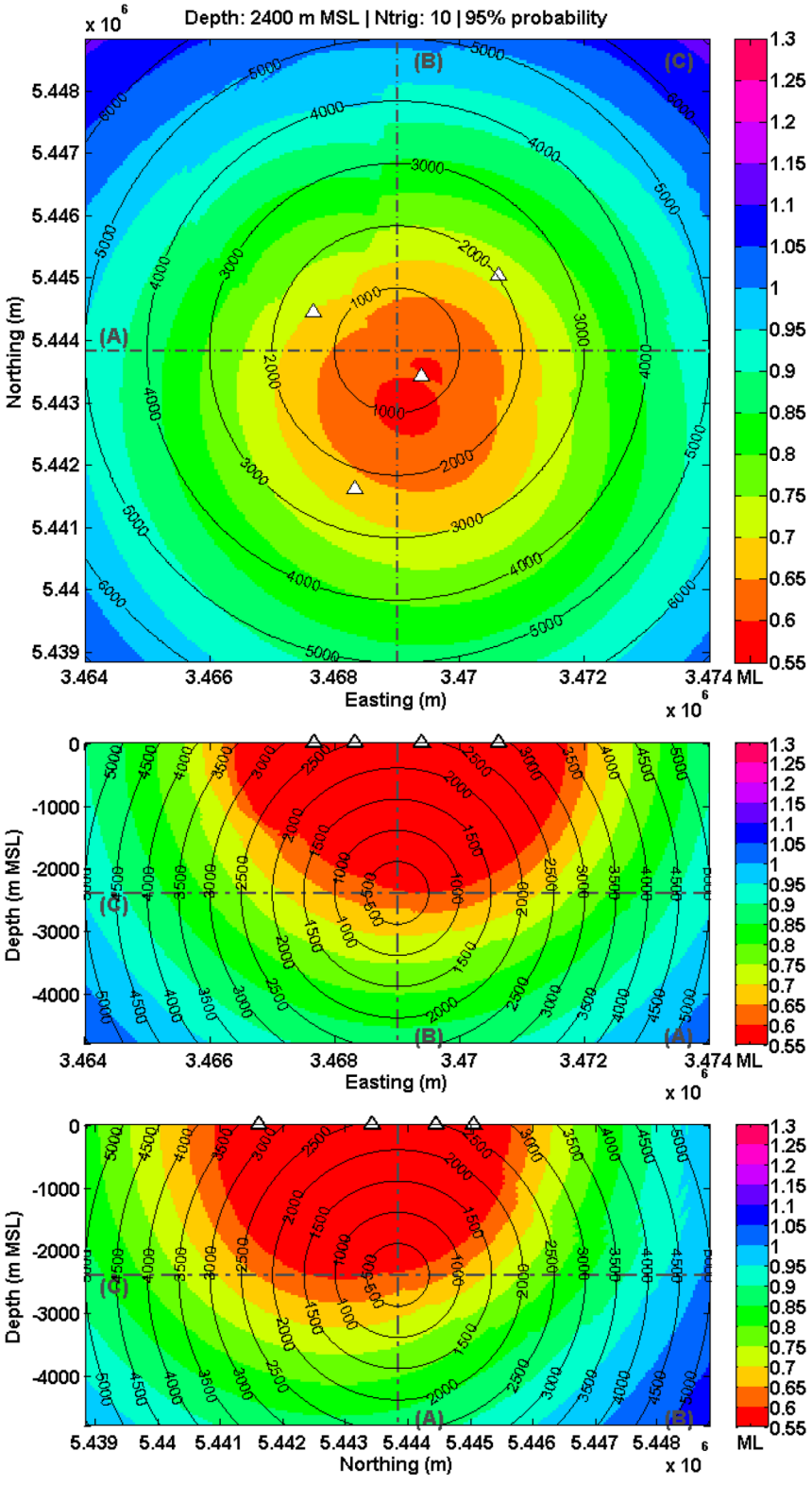

Figure 8 Detection capability of Bruchsal network, with 95% probability: horizontal section at 2400 m depth along profile (C) (top), West–East vertical section along profile (A) (middle), and South–North vertical section along profile (B) (bottom). The colour represents the minimum detectable local magnitude. The black contours give the geometrical distance from the section centre (in m). The triangles are the projection of the seismic station locations. To detect an event, ten traces among 16 must simultaneously trigger.

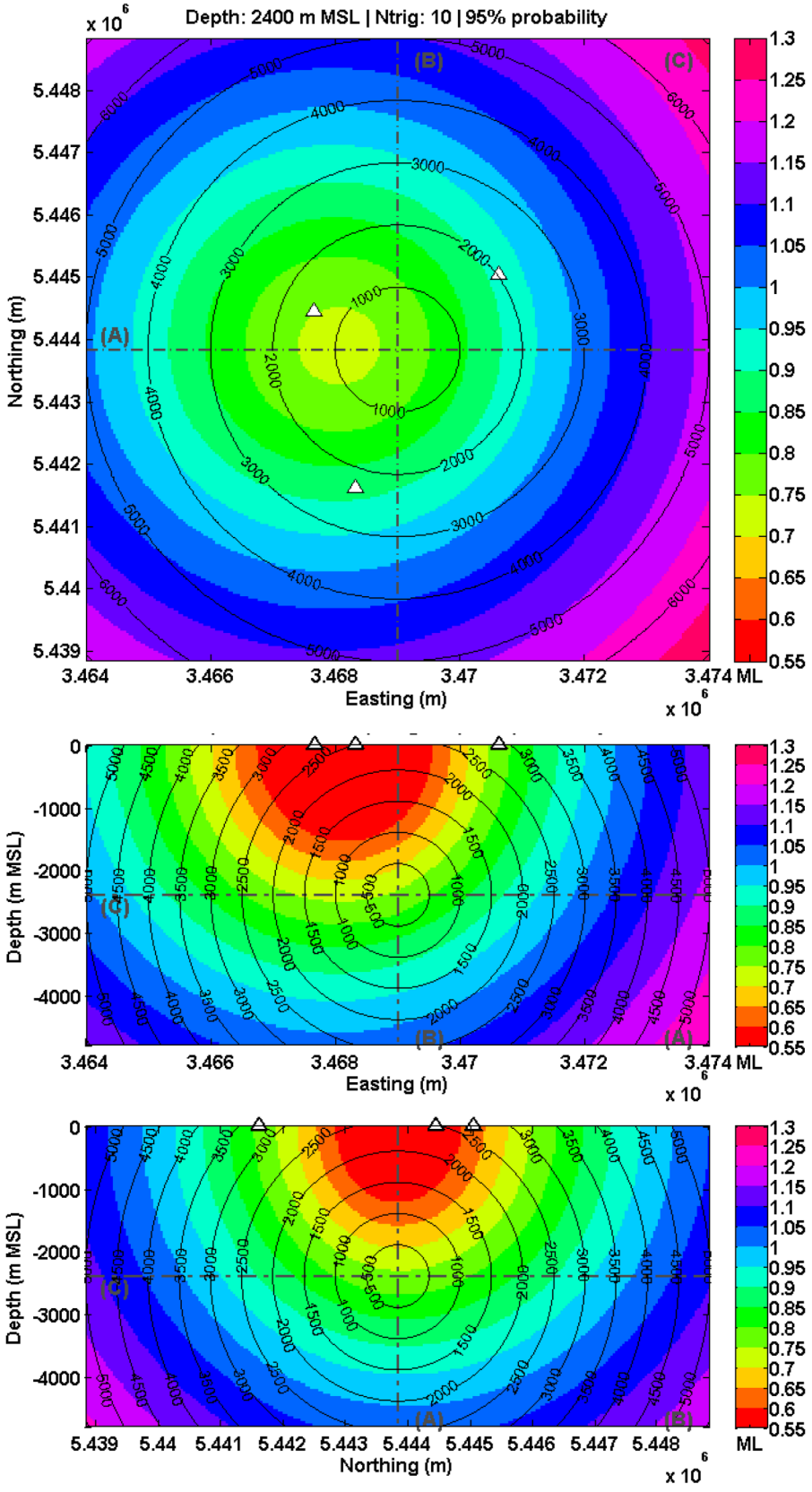

Figure 9 Same as Figure 8 but assuming that station A01, initially in the middle of the network, is removed.

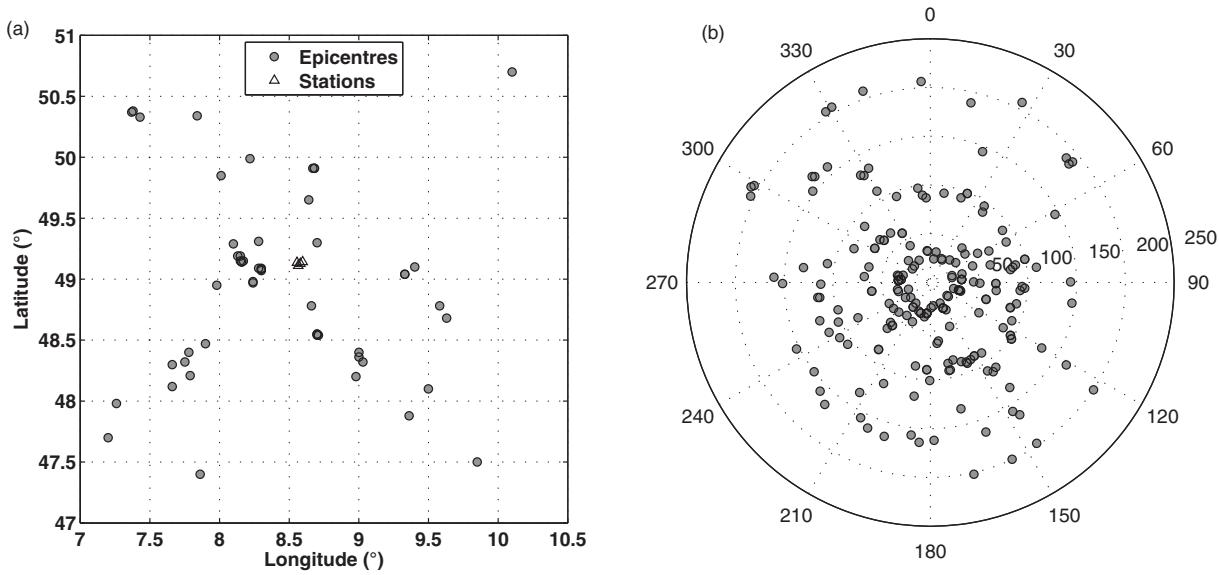

Figure 10 Left: epicentre map of all earthquakes of the catalogue used for calibrating equation (3). Right: polar distribution of the hypocentral distances (radial axis, in km) and azimuths (rotation axis, in degrees) of these earthquakes relative to each station.

optimized for each station using the new b constant. The three minimization criteria were again used and the least absolute solution kept since it provided the most robust results. The magnitude residuals were computed and compared with the original solution. As the residuals did not get smaller, the calibration was not improved by including more parameters in the optimization procedure, and the initial solution was kept.

The results must be interpreted bearing in mind the assumptions made. Although equation (3) has been calibrated from earthquakes located at least 20 km away from the network, it is extrapolated to short distances. This implies that the geometrical and intrinsic attenuation of the seismic waves is assumed to behave similarly below the network and along few-kilometre ray-paths. Moreover, the BRC earthquake depths and epicentral distances are not treated independently. Since the local geological structure of Bruchsal is complex because it underwent tectonical deformation processes leading to compartmentalization of the geothermal reservoir and vertical displacement of several blocks (Herzberger *et al.* 2010; Meixner 2010), there is a remaining uncertainty that can only be quantified when nearby induced seismic events could be recorded. Therefore, the assumption of an equivalent homogeneous model is probably inappropriate and may lead to a systematic bias. The detection capability was computed for the low-frequency branch of the detection sequence (i.e., below 25 Hz). This provided enough constraints for calibrating the magnitude–distance–amplitude relation; however, this assumes that the low-frequency branch is still suitable to detect local earthquakes below the network.

Finally, none of the local magnitude equations (1), (2), or (3) takes into account the effect of the seismic radiation pattern of the earthquakes. Consequently, that latter is averaged during calibration of equation (3) and contributes to the calculated values of the *a posteriori* misfits and σ_S. However, with the proposed probabilistic formalism (equation (4)), this effect is partly accounted for. In the same way, any assumption or lack of knowledge leading to imprecision or aleatoric uncertainties, which can be quantified in the magnitude residuals and σ_S, will be considered in this probabilistic approach.

The detection capability as computed by the current procedure relies on a detection criterion combining single trace triggering based on filtered amplitude measurements. It is not possible to apply it on the STA/LTA triggering criterion (Figure 2), because this ratio has no direct relation with the signal amplitude and cannot replace the amplitude term in equation (1). However, the STA value can be used instead of the amplitude (e.g., Ringdal and Kværna 1989; von Seggern 2004; Kværna *et al.* 2007). The proposed approach is neither applicable when matched filters, beamforming, or migration-based processing are used to jointly detect and locate earthquakes (e.g., Gibbons and Ringdal 2006; Gharti *et al.* 2010). Under these processing schemes, new approaches should be developed to avoid unrealistic and pessimistic detection scenarios.

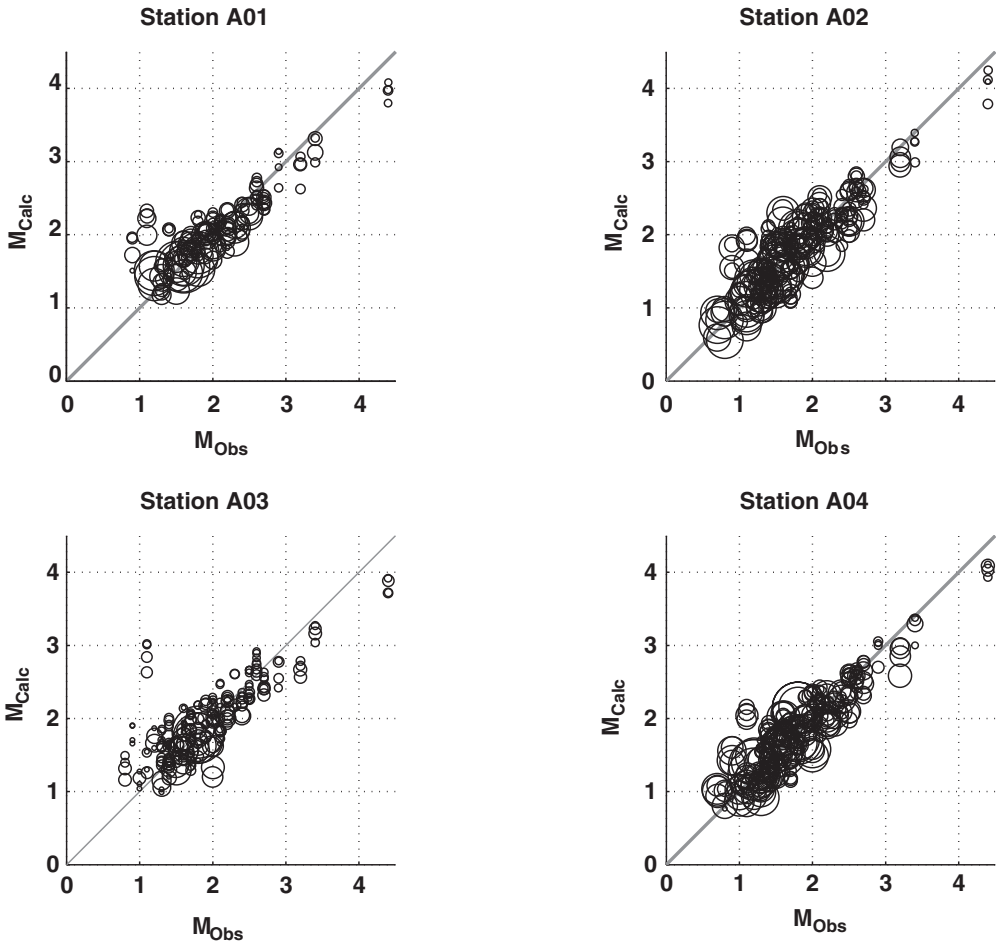

Figure 11 Magnitude calculated using the calibrated function as a function of the corresponding local magnitude in the catalogue. The size of the circle is inversely proportional to the noise measured on the detection trace. The grey line represents a perfect fit.

In a perspective view, to obtain the network capability in terms of location, it would be necessary to link location criteria with seismogram amplitude criteria. This may be done for example by requiring several body-wave phases (instead of using only the S-wave arrivals as presented) and by setting stronger criteria associated to the fixed amplitude threshold, for each seismic phase. The actual combination of the trace-dependent probabilities to compute the joint probability would change.

CONCLUSION

The observation-based method we proposed quantifies the detection capability of an existing seismic network at a local scale. This approach has three characteristics: (i) it uses the applied detection sequence, (ii) the detection capability is obtained for distances where no seismicity occurred yet, and (iii) the results take the form of probabilities. To be applied, the network should however be running for a time period long enough to detect several regional earthquakes, which are listed in a reference catalogue.

The developed methodology offers an alternative to a fully theoretical detection capability modelling and takes into consideration real field conditions. Geometrical spreading attenuation of seismic waves, intrinsic attenuation, site effect, and instrumental response are partially accounted for during the calibration of the magnitude–distance–amplitude relation. Furthermore, the probabilistic formalism considers aleatoric uncertainties due to underlying assumptions. The proposed method also differs from other catalogue-based approaches because it can still apply for distances and locations where no seismicity occurred. Moreover, it allows simulating several detection scenarios, testing the performance of the stations, and assessing the robustness of the network design.

The technique is not restricted to any specific application and is suitable for the period that follows the implementation of local networks aimed at monitoring induced seismicity. Such networks are not necessarily deployed in seismically active areas, and if the deployment occurred before any operation, the monitored zone may be seismically quiet. In such cases, knowledge of the spatial variation of the magnitude of completeness below the network is valuable to properly interpret the lack of seismicity. The Bruchsal case study is an illustration of this.

In the Bruchsal geothermal field, no seismicity closer than 20 km was recorded by the existing network between June 1, 2010, the beginning of the monitoring, and November 30, 2012. This result was confirmed by the analysis of earthquake catalogues given by reference seismological centres. After computing the network detection capability, we can state with 95% confidence that, under the current detection procedure, no seismic event with $M_L \geq 0.7$ occurred below the seismic network down to the reservoir depth, at 2400 m.

ACKNOWLEDGMENTS

This work was carried out in the frame of the LOGRO research project that was funded by the Energy Baden-Württemberg AG (EnBW) and the German Federal Ministry for the Environment, Nature Conservation and Nuclear Safety (BMU). Figure 1 was made using the Quantum GIS Geographic Information System (2013) and the background was provided by the OpenStreetMap contributors under the Open Database License (see http://www.openstreetmap.org/copyright). Figure 3 was made using the GeoMapApp 3.3.8 (see http://www.geomapapp.org) and the Global Multi-Resolution Topography from Ryan *et al.* (2009).

REFERENCES

Aki K. and Richards P.G. 1980. *Quantitative Seismology, Theory and Methods*. W.H. Freeman and Company.

Allen R. 1982. Automatic phase pickers: Their present use and future prospects. *Bulletin of the Seismological Society of America* **72**, S225–S242.

Beresnev I.A. and Atkinson G.M. 1997. Modeling finite-fault radiation from the ωn spectrum. *Bulletin of the Seismological Society of America* **87**, 67–84.

Boatwright J. 1980. A spectral theory for circular seismic sources: simple estimates of source dimension, dynamic stress drop, and radiated seismic energy. *Bulletin of the Seismological Society of America* **70**, 1–27.

Bönnemann C., Schmidt B., Ritter J., Gestermann N., Plenefisch T., Wegler U. *et al.* 2010. Das seismische Ereignis bei Landau vom 15. August 2009. In: *Abschlussbericht der Expertengruppe Seismisches Risiko bei hydrothermaler Geothermie*, pp. 55.

Bormann P. 2012. DS3.1: Magnitude calibration formulas and tables, comments on their use and complementary data. In: *New Manual of Seismological Observatory Practice (NMSOP-2), IASPEI* (ed P. Bormann), pp. 19. GFZ German Research Centre for Geosciences.

Bungum H. and Husebye E.S. 1974. Analysis of the operational capabilities for detection and location of seismic events at NORSAR. *Bulletin of the Seismological Society of America* **64**, 637–656.

Deichmann N. and Giardini D. 2009. Earthquakes induced by the stimulation of an enhanced geothermal system below Basel (Switzerland). *Seismological Research Letters* **80**, 784–798.

Del Pezzo E., Bianco F., Castellano M., Cusano P., Galluzzo D., La Rocca. M. *et al.* 2013. Detection of seismic signals from background noise in the area of Campi Flegrei: Limits of the present seismic monitoring. *Seismological Research Letters* **84**, 190–198.

EMSC. 2013. *European–Mediterranean Seismological Centre*: *Earthquake Catalogue*. (http://www.emsc-csem.org/Earthquake).

Evans J.R. and Allen S.S. 1983. A teleseism-specific detection algorithm for single short-period traces. *Bulletin of the Seismological Society of America* **73**, 1173–1186.

Freudenreich Y., Oates S.J. and Berlang W. 2012. Microseismic feasibility studies–assessing the probability of success of monitoring projects. *Geophysical Prospecting* **60**, 1043–1053.

Gharti H.N., Oye V., Roth M. and Kuhn D. 2010. Automated microearthquake location using envelope stacking and robust global optimization. *Geophysics* **75**, MA27–MA46.

Gibbons S.J. and Ringdal. F. 2006. The detection of low magnitude seismic events using array-based waveform correlation. *Geophysical Journal International* **165**, 149–166.

Gomberg J. 1991. Seismicity and detection/location threshold in the Southern Great Basin Seismic Network. *Journal of Geophysical Research: Solid Earth* **96**, 16401–16414.

Herzberger P., Muench W., Koelbel T., Bruchmann U., Schlagermann P., Hoetzl H. *et al.* 2010. The geothermal power plant Bruchsal. In: *World Geothermal Congress*.

Kværna T., Ringdal F. and Baadshaug U. 2007. North Korea's nuclear test: The capability for seismic monitoring of the North Korean test site. *Seismological Research Letters* **78**, 487–497.

Kværna T., Ringdal F., Schweitzer J. and Taylor L. 2002. Optimized seismic threshold monitoring – Part 1: Regional processing. *Pure and Applied Geophysics* **159**, 969–987.

LGB-RLP. 2013. *Rheinland-Pfalz, Landesamt für Geologie und Bergbau: Erdbebenereignisse lokal. Aktuelle Erdbebenereignisse in Rheinland-Pfalz, Baden-Württemberg und bis 1000 km Entfernung*. (http://www.lgb-rlp.de/ereignisse_lokal.html).

Meixner J. 2010. *Diplomarbeit: Konzeptionelle hydrogeologische Modellansätze als Vorstudie für ein integriertes Standortmodell*, pp. 178. KIT – Institut für Angewandte Geowissenschaften – Abteilung Hydrogeologie.

Mignan A., Werner M.J., Wiemer S., Chen C.-C. and Wu Y.-M. 2011. Bayesian estimation of the spatially varying completeness magnitude of earthquake catalogs. *Bulletin of the Seismological Society of America* **101**, 1371–1385.

QGIS. 2013. Quantum GIS Development Team. Quantum GIS Geographic Information System. Open Source Geospatial Foundation Project. (http://qgis.osgeo.org).

Richter C.F. 1935. An instrumental earthquake magnitude scale. *Bulletin of the Seismological Society of America* **25**, 1–32.

Ringdal F. 1975. On the estimation of seismic detection thresholds. *Bulletin of the Seismological Society of America* **65**, 1631–1642.

Ringdal F. and Kværna T. 1989. A multi-channel processing approach to real time network detection, phase association, and threshold monitoring. *Bulletin of the Seismological Society of America* **79**, 1927–1940.

Ringdal F. and Kværna T. 1992. Continuous seismic threshold monitoring. *Geophysical Journal International* **111**, 505–514.

Ryan W.B.F., Carbotte S.M., Coplan J.O., O'Hara S., Melkonian A., Arko R. *et al*. 2009. Global multi-resolution topography synthesis. *Geochemistry, Geophysics, Geosystems* **10**, Q03014.

Schorlemmer D. and Woessner J. 2008. Probability of detecting an earthquake. *Bulletin of the Seismological Society of America* **98**, 2103–2117.

Sereno T.J. and Bratt S.R. 1989. Seismic detection capability at NORESS and implications for the detection threshold of a hypothetical network in the Soviet Union. *Journal of Geophysical Research: Solid Earth* **94**, 10397–10414.

Stange S. 2006. ML Determination for local and regional events using a sparse network in Southwestern Germany. *Journal of Seismology* **10**, 247–257.

SZGRF-BGR. 2013. Seismological Central Observatory (BGR): Earthquakes located with GRF- and GRSN-stations. (http://www.szgrf.bgr.de/seisevents.html).

Trifu C.I. and Fehler M. 1998. Special Issue – New trends in seismological research: Studies of seismicity induced by mining, petroleum and geothermal activities. *Tectonophysics* **289**, vii–ix.

Tukey J.W. 1977. *Exploratory Data Analysis*. Addison-Wesley. ISBN 0201076160.

von Seggern D.H. 2004. Seismic background noise and detection threshold in the Southern Great Basin Digital Seismic Network. *Bulletin of the Seismological Society of America* **94**, 2280–2298.